The Astrophysical Journal Letters, 978:L21 (13pp), 2025 January 10 https://doi.org/10.3847/2041-8213/ad9c75
© 2025. The Author(s). Published by the American Astronomical Society.
OPEN ACCESS

Identification of the Optical Counterpart of the Fast X-Ray Transient EP240414a

S. Srivastav[1,10], T.-W. Chen[2,10], J. H. Gillanders[1,10], L. Rhodes[1,3,4], S. J. Smartt[1,5], M. E. Huber[6], A. Aryan[2], S. Yang[7], A. Beri[8], A. J. Cooper[1], M. Nicholl[5], K. W. Smith[5], H. F. Stevance[1,5], F. Carotenuto[1], K. C. Chambers[6], A. Aamer[5], C.R. Angus[5], M. D. Fulton[5], T. Moore[5], I. A. Smith[9], D. R. Young[5], T. de Boer[6], H. Gao[6], C.-C. Lin[6], T. Lowe[6], E. A. Magnier[6], P. Minguez[6], Y.-C. Pan[2], and R. J. Wainscoat[6]
[1] Astrophysics sub-Department, Department of Physics, University of Oxford, Keble Road, Oxford, OX1 3RH, UK; shubham.srivastav@physics.ox.ac.uk, james.gillanders@physics.ox.ac.uk
[2] Graduate Institute of Astronomy, National Central University, 300 Jhongda Road, 32001 Jhongli, Taiwan; twchen@astro.ncu.edu.tw
[3] Trottier Space Institute at McGill, 3550 Rue University, Montreal, Quebec H3A 2A7, Canada
[4] Department of Physics, McGill University, 3600 Rue University, Montreal, Quebec H3A 2T8, Canada
[5] Astrophysics Research Centre, School of Mathematics and Physics, Queen's University Belfast, Belfast, BT7 1NN, UK
[6] Institute for Astronomy, University of Hawai'i, 2680 Woodlawn Drive, Honolulu, HI 96822, USA
[7] Henan Academy of Sciences, Zhengzhou 450046, Henan, People's Republic of China
[8] Indian Institute of Science Education and Research (IISER) Mohali, Punjab 140306, India
[9] Institute for Astronomy, University of Hawai'i, 34 Ohia Ku Street, Pukalani, HI 96768-8288, USA
Received 2024 September 30; revised 2024 December 05; accepted 2024 December 05; published 2025 January 8

Abstract

Fast X-ray transients (FXTs) are extragalactic bursts of X-rays first identified in archival X-ray data and are now routinely discovered in real time by the Einstein Probe, which is continuously surveying the night sky in the soft (0.5–4 keV) X-ray regime. In this Letter, we report the discovery of the second optical counterpart (AT 2024gsa) to an FXT (EP 240414a). EP 240414a is located at a projected radial separation of 27 kpc from its likely host galaxy at $z = 0.4018 \pm 0.0010$. The optical light curve of AT 2024gsa displays three distinct components. The initial decay from our first observation is followed by a rebrightening episode, displaying a rapid rise in luminosity to an absolute magnitude $M_r \sim -21$ after two rest-frame days. While the early optical luminosity and decline rate are similar to those of luminous fast blue optical transients, the color temperature of AT 2024gsa is distinctly red and we show that the peak flux is inconsistent with a thermal origin. The third component peaks at $M_i \sim -19$ at $\gtrsim$16 rest-frame days post-FXT, and is compatible with an emerging supernova. We fit the *riz*-band data with a series of power laws and find that the decaying components are in agreement with gamma-ray burst afterglow models, and that the rebrightening may originate from refreshed shocks. By considering EP 240414a in context with all previously reported known-redshift FXT events, we propose that Einstein Probe FXT discoveries may predominantly result from (high-redshift) gamma-ray bursts, and thus appear to be distinct from the previously discovered lower-redshift, lower-luminosity population of FXTs.

Unified Astronomy Thesaurus concepts: Transient sources (1851); X-ray transient sources (1852); Optical identification (1167); Relativistic jets (1390); Gamma-ray bursts (629)

Materials only available in the online version of record: machine-readable table

1. Introduction

Fast X-ray transients (FXTs) are extragalactic, short duration bursts of X-rays lasting a few seconds to thousands of seconds, typically not associated with a higher- (i.e., gamma-ray) or lower- (i.e., optical, radio) energy counterpart. The field of FXTs is undergoing a revolution since the launch and operation of the Einstein Probe (EP; W. Yuan et al. 2022) in early 2024. The wide field of view (3600 deg^2 instantaneous) allows the sky to be surveyed multiple times in a 24 hr period with the wide-field X-ray Telescope on board the Einstein Probe (EP-WXT). Its lobster-eye technology typically provides a localization of 3′ radius in the soft X-ray band of 0.5–4 keV (e.g., C. Zhang et al. 2024; 2024), with a sensitivity of 1.2×10^{-10} erg s^{-1} cm^{-2} for an exposure of 100 s (W. Yuan et al. 2022). The survey power is illustrated by the grasp of the EP-WXT (effective area × field of view) being a factor of 10 greater than XMM-Newton, ROSAT, and eROSITA (see Figure 10 of W. Yuan et al. 2022). EP's follow-up X-ray telescope (EP-FXT) can be triggered to follow up and improve the localization of sources from the EP-WXT to a much smaller radius of about 10″, while also being significantly more sensitive.

Einstein Probe has released 27 discoveries[11] of candidate extragalactic FXTs through General Coordinates Network notices (GCNs) as well as a number of likely Galactic sources such as EPW 20240305aa (Y. Liu et al. 2024a, 2024b; I. M. Monageng et al. 2024; spatially consistent with a stellar source) and EP 240309a (Z. X. Ling et al. 2024; a known variable X-ray source). To uncover the nature of these FXTs, the key piece of information required is the luminosity distance, which requires the detection of an optical counterpart and a spectrum to determine redshift. Of the 27 extragalactic FXTs reported via GCNs, optical counterparts have been detected for 8, and redshifts have been measured for 5. The first counterpart discovered was that of EP 240315a (AT 2024eju;

[10] These authors contributed equally.

[11] As of 2024 August 14.

Original content from this work may be used under the terms of the Creative Commons Attribution 4.0 licence. Any further distribution of this work must maintain attribution to the author(s) and the title of the work, journal citation and DOI.

J. H. Gillanders et al. 2024), which had a remarkably high redshift of $z = 4.859$ (J. H. Gillanders et al. 2024; Levan et al. 2024b; Liu et al. 2024c) and was associated with GRB 240315C (J. DeLaunay et al. 2024; Y. Liu et al. 2024c; D. Svinkin et al. 2024). Seven of these 27 FXTs have a spatial and temporal coincidence with a gamma-ray burst (GRB). The detections and limits obtained thus far indicate that FXT counterparts are typically fainter than 20–21 mag. Apart from the high redshift of EP 240315a/AT 2024eju/GRB 240315C, the other FXTs with redshifts lie in between $0.4 \lesssim z \lesssim 3.6$ (P. G. Jonker et al. 2024; J. Quirola-Vásquez et al. 2024a, 2024b), with the next highest being EP 240804a at $z = 3.662$ (A. Bochenek et al. 2024). This may indicate that the majority of EP FXTs discovered to date, and potentially most that will be discovered by the mission, are bright X-ray counterparts to high-redshift GRBs, and thus EP observations may signpost a method to locate distant explosions for rapid follow-up observations. The 3′ error radius provided by EP-WXT enables many facilities to quickly and sensitively search for optical counterparts.

Before the launch of EP, FXTs had been discovered in archival images from the more sensitive and narrower-field-of-view missions Chandra and XMM-Newton (P. G. Jonker et al. 2013; A. Glennie et al. 2015; F. E. Bauer et al. 2017). Twelve FXTs uncovered in XMM-Newton data were reported by D. Alp & J. Larsson (2020), and D. Eappachen et al. (2024) showed the spectroscopic redshifts of seven plausible hosts lie in the range $0.098 < z < 0.645$. Supernova shock breakout (SBO) from blue and red supergiants, or from Wolf–Rayet progenitors surrounded by a dense circumstellar medium, has been suggested as the origin for these archival FXTs by D. Alp & J. Larsson (2020), although the higher redshifts of the putative hosts now challenge that interpretation. Other explanations proposed for these FXTs are binary neutron star (BNS) mergers producing a magnetar central engine (Y. Q. Xue et al. 2019; S. Ai & B. Zhang 2021; N. Sarin et al. 2021; D. Eappachen et al. 2023; J. Quirola-Vásquez et al. 2024c) and the tidal disruption of white dwarfs by intermediate-mass black holes (M. MacLeod et al. 2016).

The extensive search through over 22 yr of Chandra archival data by J. Quirola-Vásquez et al. (2022, 2023) is now providing sky rates and quantifying the X-ray fluxes and durations of FXTs. Given that EP FXTs are typically 100–1000 times brighter than the Chandra and XMM-Newton sources, the link between the two populations is an open question. The large X-ray fluxes, high redshifts, and GRB coincidences of the EP-detected FXTs to date are in contrast to the fainter and lower-redshift Chandra and XMM-Newton objects.

In this Letter, we present the optical counterpart discovery and follow-up to the FXT EP 240414a, which, to date, has the lowest redshift of any counterpart to an extragalactic EP source. As such, it may provide insight into the links between these two populations. EP 240414a was detected on 2024 April 14 at 09:50:12 UTC (MJD 60414.40986) by the wide-field X-ray telescope with a peak flux $f_X \sim 3 \times 10^{-9}$ erg s^{-1} cm^{-2} in the 0.5–4 keV band (T. Y. Lian et al. 2024). A counterpart and host galaxy were quickly reported (A. Aryan et al. 2024a), followed by a redshift of the host ($z \simeq 0.41$; P. G. Jonker et al. 2024). Remarkably, the optical counterpart was observed to rebrighten (S. Srivastav et al. 2024), a signature of a supernova (SN) was reported (A. J. Levan et al. 2024a), and a luminous radio counterpart was also reported (J. Bright et al. 2024a).

Throughout this paper we assume ΛCDM cosmology with a Hubble constant $H_0 = 67.7$ km s^{-1} Mpc^{-1}, $\Omega_M = 0.309$, and $\Omega_\Lambda = 0.691$ (Planck Collaboration et al. 2016). We also assume a line-of-sight Milky Way extinction of $E(B - V) = 0.033$ mag (E. F. Schlafly & D. P. Finkbeiner 2011).

2. Discovery of the Optical Counterpart with LOT

The 3′ uncertainty in the position of EP 240414a and the discovery time provided by EP-WXT (T. Y. Lian et al. 2024) offered the opportunity for the telescopes at the Lulin Observatory in Taiwan to search for a counterpart within the first few hours of the FXT alert. As part of our ongoing program of fast response follow-up for multiwavelength and multimessenger transients at Lulin (Kinder; see T. W. Chen et al. 2021; T.-W. Chen et al. 2024), we observed the field of EP 240414a using the Lulin One-meter Telescope (LOT). The LOT is equipped with a 2048 × 2048 pixel CCD, providing a 12′ field of view, and a set of Sloan Digital Sky Survey (SDSS) $u'g'r'i'z'$ filters. The first LOT epoch of observations started on 2024 April 14 at 12:58 UTC (MJD 60414.540), 3.12 hr following the EP trigger. We obtained a sequence of 6 × 300 s images, alternating between the r and i filters. Approximately three hours later, we conducted observations in the g band, following the same 6 × 300 s sequence. The transient was clearly identified by eye in the first set of coadded r-band images.

The data were processed in a standard manner; images were stacked and template images from the Legacy Survey DR10 (A. Dey et al. 2019) were used as reference to produce difference images for rapid transient searches (see S. Yang et al. 2021 for a description of the pipeline). The new optical transient, AT 2024gsa, was discovered in the difference images (A. Aryan et al. 2024a), and was reported to the Transient Name Server (A. Aryan et al. 2024b) with coordinates R.A. $= +12^h46^m01\overset{s}{.}67$, decl. $= -09°43'08\overset{''}{.}8$. We measured discovery magnitudes of $r = 21.52 \pm 0.12$ and $i = 21.40 \pm 0.16$ (AB mag). The two nearest cataloged optical sources in the SDSS DR15 (D. S. Aguado et al. 2019), the Pan-STARRS1 3π survey DR2 (H. A. Flewelling et al. 2020), and the DESI Legacy Surveys DR10 (A. Dey et al. 2019) are $3\overset{''}{.}6$ and $4\overset{''}{.}9$ offset from AT 2024gsa. The nearest source, SDSS J124601.74-094312.1, is morphologically classified as a stellar object ($r = 20.27 \pm 0.03$ AB mag) in both SDSS DR15 and the Legacy Survey DR10. The most likely host is the brighter ($r = 19.04 \pm 0.02$ AB mag) galaxy to the east, SDSS J124601.99−094309.3, with coordinates R.A. $= 12^h46^m01\overset{s}{.}99$, decl. $= -09°43'09\overset{''}{.}34$. AT 2024gsa has a projected $4\overset{''}{.}9$ offset from this galaxy, which has a photometric redshift of $z = 0.299 \pm 0.043$ from SDSS DR15. The discovery images and the host galaxy are shown in Figure 1.

This source was confirmed as the likely counterpart with the 2.56 m Nordic Optical Telescope at 12.29 hr after the EP trigger (D. Xu et al. 2024), and a spectrum taken at approximately +15 hr by P. G. Jonker et al. (2024) indicated a featureless continuum and a redshift of $z = 0.41$ for the most likely host galaxy SDSS J124601.99−094309.3.

Following discovery, we launched a multiwavelength observing campaign to sample the evolution of the optical counterpart; for details of our observing campaign, see Appendix A. Our optical light curve is presented in Figure 3 and the summary of photometric observations is provided in

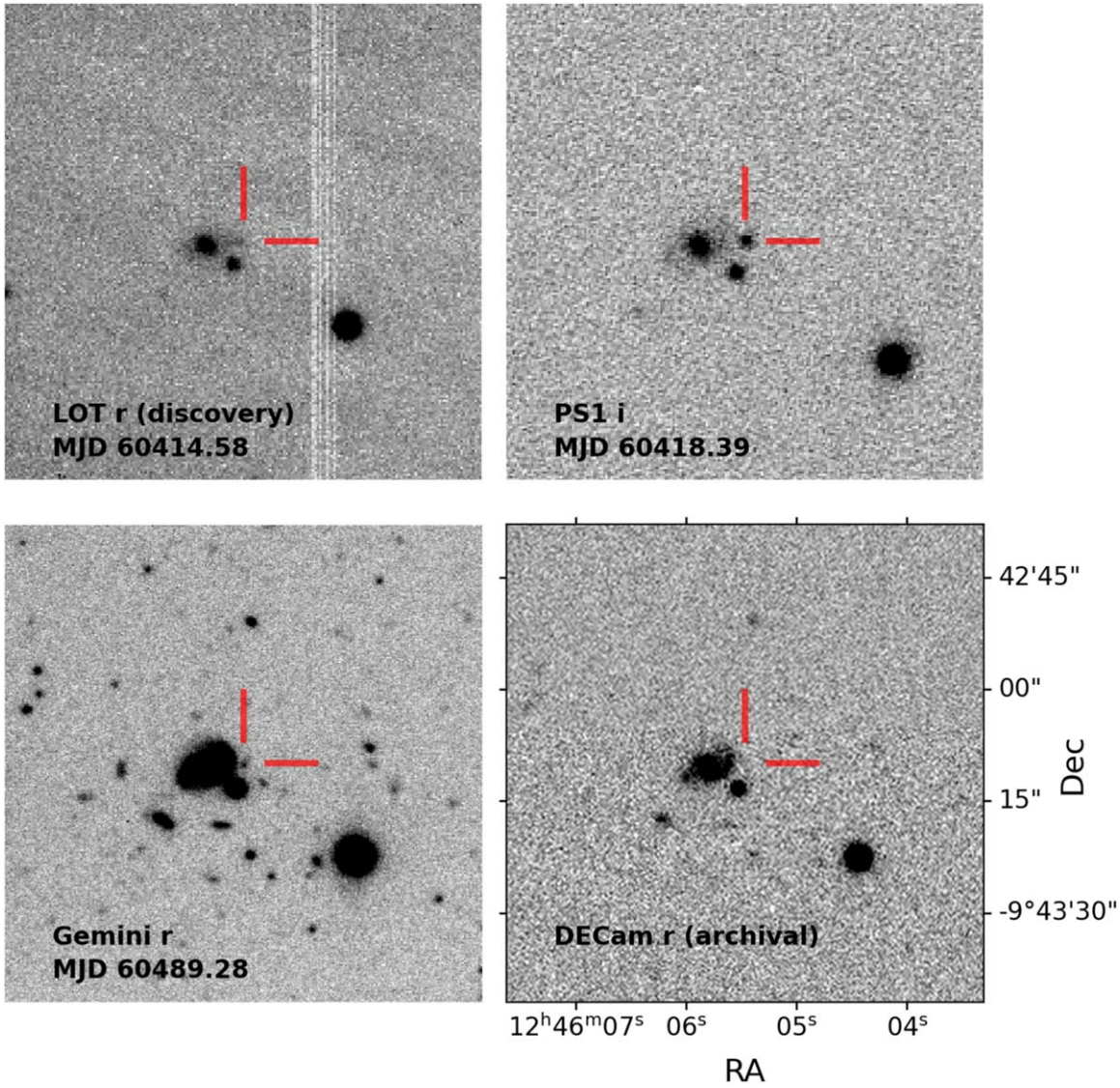

Figure 1. LOT discovery image of AT 2024gsa, along with follow-up images obtained with Pan-STARRs1 (PS1) and Gemini. Also shown (bottom right) is an archival image of the field from the Dark Energy Survey Camera (DECam).

Table 1. We also present the Swift/XRT data and use it to constrain the optical-to-X-ray spectral energy distribution.

3. Spectroscopic Observation with Gemini and Host Redshift Measurement

With a Gemini-South Director's Discretionary Time proposal (PI: S. J. Smartt), we were awarded time for long-slit spectroscopy of the transient and its host galaxy. However, due to weather and instrument availability constraints we could only observe once the transient had faded from detectability. We centered the slit of the Gemini Multi-object Spectrograph (GMOS-S) on the host galaxy SDSS J124601.99−094309.3, with a slit angle of 95°.2 east of north. This was to capture the position of AT 2024gsa at a separation of 4.″9 (see Figure 1) from the host. We obtained 4 × 1800 s exposures on 2024 July 17 (commencing at 23:17:27 UT/MJD 60508.970) with the R400 grism, the GG455 blocking filter, and a 1.″0 slit width. Dithering was employed in both the spatial (15.″0, for sky subtraction) and wavelength (200 Å, to cover the chip gaps) directions.

We used the DRAGONS pipeline (K. Labrie et al. 2023a, 2023b) to reduce the data following standard recipes, with the reduced spectrum flux-calibrated against a standard star. This produced the combined, stacked spectrum shown in Figure 2. Strong emission lines of Hα, Hβ, [N II] $\lambda\lambda$6548.050, 6583.460, [S II] $\lambda\lambda$6716.440, 6730.810, [O III] $\lambda\lambda$4958.911, 5006.843, and [Ar III] λ7135.790 are observed at a common redshift of $z = 0.4018 \pm 0.0010$. In comparison, the photometric redshift of the host from SDSS DR15 was estimated to be $z_{\rm phot} = 0.299 \pm 0.043$ (D. S. Aguado et al. 2019). At a redshift of $z = 0.4018$, the luminosity distance and distance modulus derived assuming ΛCDM cosmology (as outlined in Section 1; see also Planck Collaboration et al. 2016) are $D_{\rm L} = 2.25$ Gpc and $\mu = 41.76$, respectively. The angular scale is 5.55 kpc arcsec^{-1}, implying a projected physical separation of $R_g = 27$ kpc between the host galaxy and the position of AT 2024gsa. The slit position of GMOS-S was oriented to include the position of AT 2024gsa at a separation of 4.″9. There is no detection of any continuum or emission line flux at the position of EP 240414a/AT 2024gsa (see Figure 2).

Table 1
Optical Photometry of AT 2024gsa

MJD	$T_{\rm mid} - T_0$ (Observer-frame Days)	Telescope	Filter	Total Exposure Time (s)	Apparent Magnitude (AB mag)	Error (AB mag)
60414.58	0.17	LOT	*r*	3300	21.55	0.08
60414.60	0.19	LOT	*i*	3600	21.40	0.16
60414.75	0.34	LOT	*g*	1800	21.90	0.12
60415.61	1.20	LOT	*i*	1500	21.69	0.23
60415.64	1.23	LOT	*r*	5700	22.05	0.07
60416.40	1.99	PS	*r*	900	>22.40	⋯
60416.41	2.00	PS	*i*	900	22.37	0.19
60416.42	2.01	PS	*z*	900	21.95	0.20
60416.56	2.15	LOT	*r*	6000	22.05	0.14
60416.64	2.23	LOT	*i*	5400	22.20	0.15
60417.38	2.97	PS	*i*	1200	20.86	0.05
60417.40	2.99	PS	*z*	1200	20.56	0.06
60417.51	3.10	LOT	*r*	3300	21.06	0.15
60418.39	3.98	PS	*z*	600	20.30	0.06
60418.39	3.98	PS	*i*	600	20.51	0.06
60418.40	3.99	PS	*r*	600	20.75	0.08
60418.41	4.00	PS	*g*	600	21.08	0.12
60419.36	4.95	PS	*i*	400	20.97	0.09
60419.37	4.96	PS	*y*	200	20.55	0.27
60419.37	4.96	PS	*z*	400	20.77	0.09
60419.38	4.97	PS	*r*	480	21.11	0.31
60419.39	4.98	PS	*g*	480	> 20.57	⋯
60420.37	5.96	PS	*i*	900	21.30	0.27
60420.38	5.97	PS	*z*	900	21.31	0.24
60432.36	17.95	PS	*r*	900	22.89	0.21
60432.37	17.96	PS	*i*	900	22.29	0.21
60432.38	17.97	PS	*z*	900	22.32	0.26
60436.37	21.96	PS	*r*	800	> 22.49	⋯
60436.38	21.97	PS	*i*	800	22.16	0.31
60436.39	21.98	PS	*z*	1200	22.02	0.31
60455.28	40.87	PS	*i*	1600	23.16	0.29
60455.30	40.89	PS	*z*	1600	22.63	0.22
60459.28	44.87	PS	*i*	1600	23.35	0.35
60459.30	44.89	PS	*z*	1600	22.65	0.21
60463.28	48.87	PS	*i*	1600	23.39	0.33
60463.30	48.89	PS	*z*	1600	22.67	0.25
60467.28	52.87	PS	*i*	1600	23.36	0.31
60467.30	52.89	PS	*z*	1600	23.14	0.32
60489.28	74.87	Gemini-North	*r*	1260	24.28	0.27
60489.30	74.89	Gemini-North	*i*	1260	23.76	0.28
60489.32	74.91	Gemini-North	*z*	1080	23.05	0.27
60507.98	93.57	Gemini-South	*i*	870	> 24.58	⋯

Note. Reported magnitudes are not corrected for the foreground Galactic extinction of $E(B-V) = 0.033$ AB mag (E. F. Schlafly & D. P. Finkbeiner 2011). The errors for the optical photometry are quoted to 1σ, and upper limits are 3σ. T_0, the time of trigger for EP 240414a, is MJD 60414.40986.

(This table is available in its entirety in machine-readable form in the online article.)

Finally, we estimate the chance coincidence of EP 240414a/AT 2024gsa with SDSS J124601.99−094309.3 using the procedure outlined by J. S. Bloom et al. (2002). We find that the probability of chance coincidence is $\lesssim$0.01, indicating that the transient is almost certainly located at $z = 0.4018$, and is indeed associated with SDSS J124601.99−094309.3 (see also J. N. D. van Dalen et al. 2024 for additional observational evidence in favor of a $z \simeq 0.40$ location).

4. Light-curve Analysis

The optical light curve of AT 2024gsa is shown in Figure 3. The shaded regions highlight distinct phases in the light-curve evolution. Phase A represents the rapidly declining early light curve lasting ∼1.5 rest-frame days post-FXT. AT 2024gsa was discovered a few hours following the FXT (see Section 2) with a luminosity of $M_r \approx -20$ (AB mag).

We consider the possibility of phase A resulting from a cooling tail following shock breakout from an extended stellar envelope (E. Waxman & B. Katz 2017), although this interpretation is not supported by the high luminosity and red color ($g - i \approx 0.4$; observer frame). Moreover, the 0.4–4 keV X-ray flux reported by EP (T. Y. Lian et al. 2024) implies an X-ray luminosity of $\sim 10^{48}\,{\rm erg\,s^{-1}}$, 2 orders of magnitude higher than the candidate SN shock breakout events identified by D. Alp & J. Larsson (2020). Since shock breakout emission is thermal in nature, the combination of high X-ray luminosity and red optical color is inconsistent with this interpretation.

Phase B (spanning ∼1.5–10 rest-frame days) highlights an abrupt, rapid, and achromatic rise in flux by a factor of $\gtrsim$3,

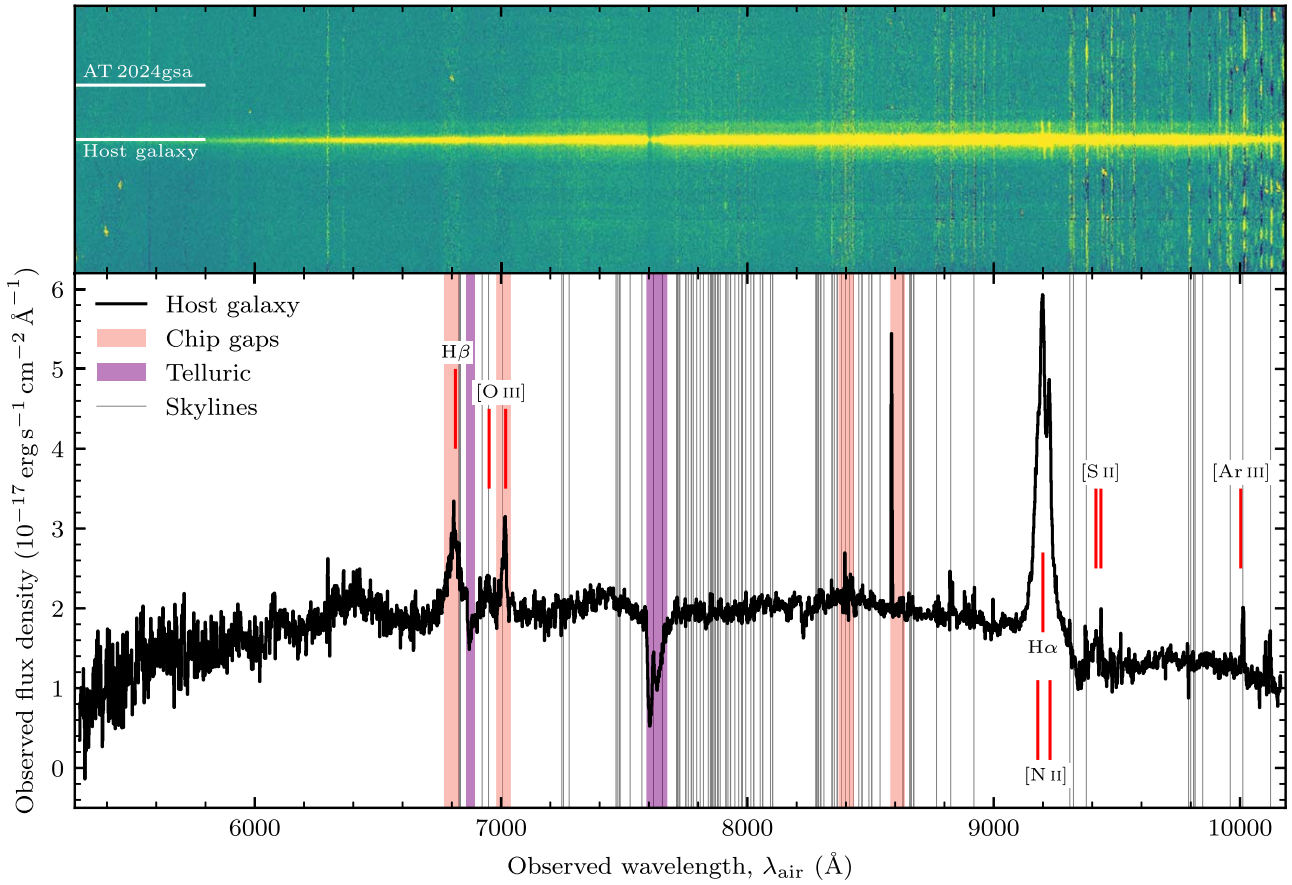

Figure 2. Upper panel: 2D Gemini-South GMOS-S spectrum of AT 2024gsa and its host galaxy, SDSS J124601.99−094309.3. The location of the host galaxy and transient traces are marked. Lower panel: 1D spectrum of the host galaxy of AT 2024gsa. The prominent emission features from which we extract a redshift estimate are marked and labeled. Regions corresponding to chip gaps and telluric absorption are shaded, and prominent sky lines (from R. W. Hanuschik 2003) are overlaid.

followed by a fast decline. The rapid timescale (∼2 days rise) and absolute magnitude (~ -21 AB mag) during the peak of phase B bears resemblance to the observed characteristics of luminous fast blue optical transients (LFBOTs; e.g., D. A. Perley et al. 2019). However, the red color of AT 2024gsa during phase B's peak ($r - z \approx 0.4 \pm 0.1$; observer frame) is at odds with LFBOTs. The middle panels in Figure 3 show light-curve comparisons between AT 2018cow (S. J. Prentice et al. 2018) and AT 2024gsa. Given the redshift of the likely host galaxy for AT 2024gsa ($z = 0.4018$; see Section 3), we plot the observed *riz* light curves of AT 2024gsa alongside the *gri* light curves of AT 2018cow, respectively, for a more meaningful comparison. Although the timescales for the *riz* (*gri*) light curves for AT 2024gsa (AT 2018cow) are similar, AT 2024gsa is significantly more luminous at peak in the redder *iz* bands, highlighting the intrinsically red color in stark contrast to AT 2018cow and LFBOTs in general.

Assuming the phase B peak is thermally driven, the absolute magnitude $M_r \approx -21$ would imply a luminosity $L \simeq 8 \times 10^{43}$ erg s^{-1} (with zero bolometric correction). We fit the *riz*-band photometry during phase B with the `SuperBol` code (M. Nicholl 2018). `SuperBol` converts the extinction-corrected broadband photometry into monochromatic fluxes and performs a blackbody fit (redshift effects are accounted for). We infer a blackbody temperature $T_{bb} \approx 8000 \pm 2000$ K for AT 2024gsa around phase B peak. The large uncertainty on the temperature is due to the fact that the blackbody fit is performed on only three optical bands. The inferred luminosity around phase B peak, integrated across just the *gri* bands, is $L_{gri} \approx 2.5 \times 10^{43}$ erg s^{-1}, whereas the total luminosity integrated over the extrapolated blackbody fit is $L_{bb} \approx 8.5 \times 10^{43}$ erg s^{-1}. The fit yields a photospheric radius $R_{bb} \approx 5 \times 10^{15}$ cm. This radius is very large for a compact progenitor origin, thus requiring an extreme ejecta velocity ($v_{ej} \sim 0.7$ c), given the rapid timescale of ∼3 days to (phase B) peak. Although the radius may be plausible for an extended stellar envelope or circumstellar material distribution, as alluded to earlier, the combination of luminous X-ray emission and red optical colors seems to rule out a thermal emission mechanism. This is further illustrated by the requirement of $E_{kin} \gtrsim 4 \times 10^{52}$ erg to eject just $0.1\,M_\odot$ at this velocity. Thermal emission models for AT 2018cow and other LFBOTs can reproduce the observed light curves as they are extremely hot ($T_{bb} \simeq 30{,}000$ K) at peak. The red color of AT 2024gsa makes this explanation untenable for the observed peak at ∼3 days. We present a color comparison for AT 2024gsa with AT 2018cow, GRB 071010A, and SN 1998bw in Appendix B and Figure 6. This illustrates the red color of AT2024gsa, and, while the early color evolution may be similar to that of SN 1998bw, the very high luminosity requires a large photospheric radius and thus an extreme ejecta velocity, as described above.

Based on these simple calculations, we undertake a more robust analysis of the phase B light curve of AT 2024gsa using the publicly available Modular Open Source Fitter for Transients (`MOSFiT`; M. Nicholl et al. 2017; J. Guillochon

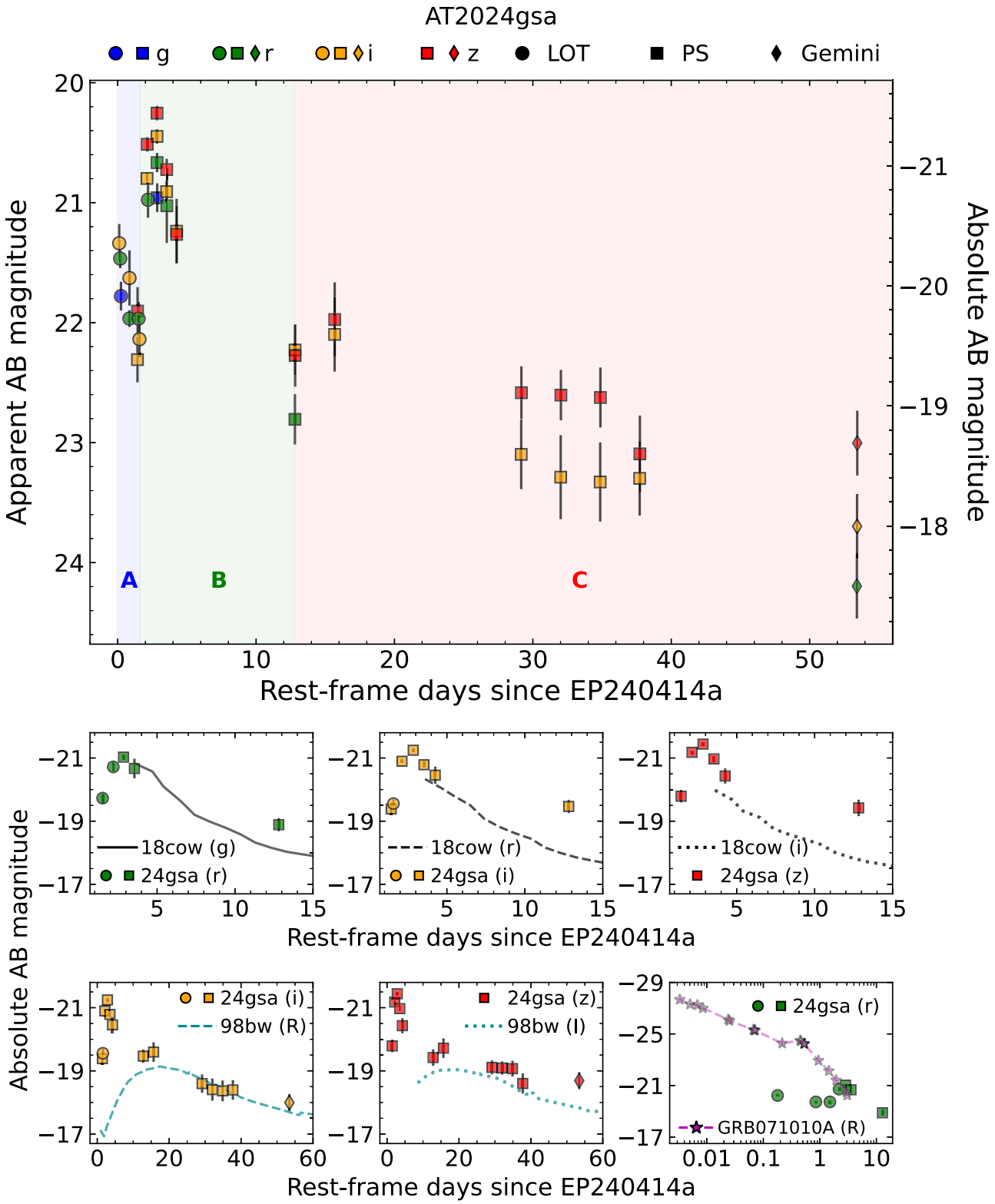

Figure 3. Upper panel: multiband optical (*griz*) light curves of AT 2024gsa obtained with LOT, Pan-STARRS, and Gemini. Both apparent and absolute magnitude scales are shown. The shaded regions highlight the three distinct phases in the optical light curve. Middle panels: comparison of the rapidly evolving phase B of AT 2024gsa with the well-studied FBOT AT 2018cow (S. J. Prentice et al. 2018). Lower-left and center panels: comparison of the slowly evolving phase C of AT 2024gsa with the broad-line Ic SN 1998bw (A. Clocchiatti et al. 2011). Lower-right panel: comparison of AT 2024gsa (*r* band) at early times with the *R*-band light curve of GRB 071010A, which exhibited a rebrightening episode ≈0.6 day post-GRB (S. Covino et al. 2008).

et al. 2018). We attempt to fit three models—the `default` model powered by the radioactive decay of ^{56}Ni (D. K. Nadyozhin 1994), the `magni` model combining the luminosity from ^{56}Ni decay and energy injection from the spin-down of a rapidly rotating magnetar (D. Kasen & L. Bildsten 2010), and the `magnetar` model powered only by the magnetar

component. The `default` model produces the poorest fit, which is expected given the combination of high luminosity and rapid timescale involved. Although the magnetar-driven models yield better fits to the light curve, all models require extreme ejecta velocities in the range $0.8 \lesssim v_{ej}/c \lesssim 0.9$. As highlighted in the order-of-magnitude calculations above, this is owing to the intrinsically red color of AT 2024gsa that forces the model to converge to a low effective temperature. The high luminosity can thus only be explained by a large photospheric radius, thereby leading to very high expansion velocities. Based on these arguments, we deem these models to be unphysical. The overall characteristics of the light curve, including the high luminosity, rapid evolution, red color, and achromaticity, suggest a nonthermal powering mechanism instead as the most likely explanation.

In the bottom-right panel of Figure 3, we compare the *r*-band light curve of AT 2024gsa with *R*-band observations of the afterglow of GRB 071010A (S. Covino et al. 2008). The GRB 071010A afterglow exhibited an achromatic and abrupt rebrightening episode ≈0.6 rest-frame days post-GRB, slightly earlier than the rebrightening observed in AT 2024gsa. Late-time rebrightening episodes such as the one observed in GRB 071010A are not unheard of in GRB afterglow light curves, and are often attributed to additional energy injection from refreshed shocks (M. J. Rees & P. Mészáros 1998). We discuss this interpretation in more detail in Section 5.1.

Finally, the third phase that we define for the light curve (phase C) appears to show marginal evidence for a rising component after ∼12 rest-frame days, although our photometric coverage at these epochs was affected by the Moon and adverse weather. Nevertheless, it is clear that the rapid initial evolution during phases A and B has slowed down at these later epochs. The timescale and absolute magnitude for the *iz*-band light curves of AT 2024gsa at this phase are compatible with an emerging SN component. Broad-line Ic supernovae (SNe) are often found in association with long GRBs. In the bottom panels of Figure 3, we compare the *iz* light curve of AT 2024gsa with the *RI* light curves of the broad-line Ic SN 1998bw (A. Clocchiatti et al. 2011) associated with GRB 980425 (S. E. Woosley et al. 1999). The comparison shows that the presence of an underlying SN component is plausible, supporting a long-duration GRB interpretation for EP 240414a (see also J. S. Bright et al. 2024b; J. N. D. van Dalen et al. 2024). However, the lack of multiband, high-cadence photometric coverage during phase C limits any definitive conclusions.

5. Discussion

5.1. The Nature of EP 240414a/AT 2024gsa

Given the findings and conclusions drawn in Section 4, we examine the optical light curves and spectra of AT 2024gsa in the context of external shock models.

The most striking signature of the optical light curves is the very rapid rise between 1.5 and 3 rest-frame days post-FXT. For the bands where we have the most comprehensive coverage (*riz*), we connect the points either side of the sharp rise between 2 and 3 days with a simple power-law model (no observations were made during the rise). We measure temporal indices of 2.4 ± 0.5, 4.1 ± 0.5, and 3.1 ± 0.5 for the *r*, *i*, and *z* bands, respectively.

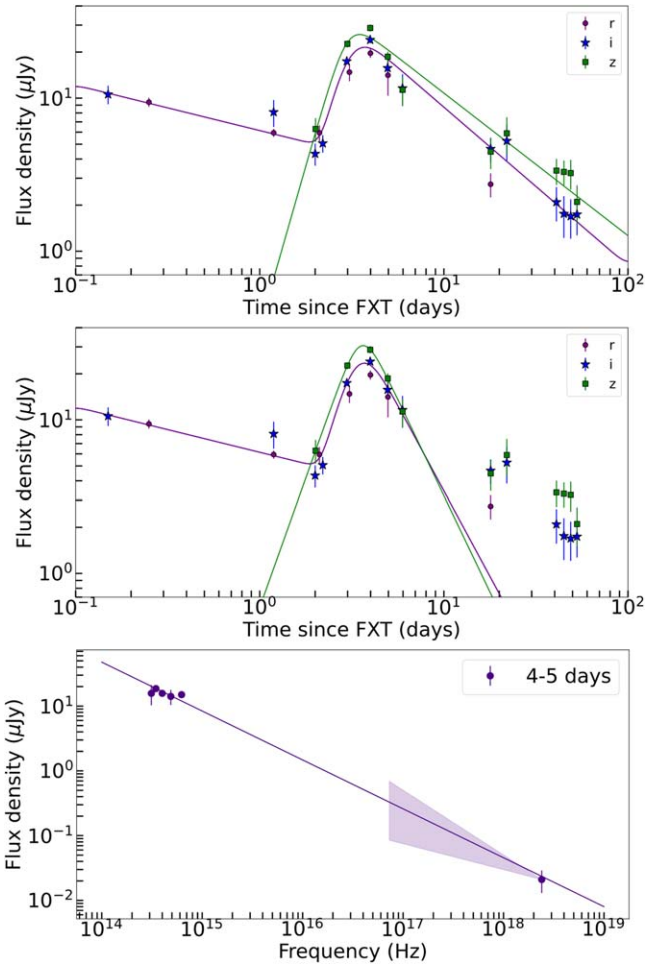

Figure 4. Top panel: power law + broken power law fits to the full *riz*-band data for AT 2024gsa. Temporal indices during the initial decay around phase A are $\alpha_1 = -0.31 \pm 0.02$ and -0.33 ± 0.05 for *r* and *i* bands, respectively. The indices for the post-peak decline are $\alpha_3 = -1.4 \pm 0.4$, -1.04 ± 0.07, and -0.93 ± 0.09 for *r*, *i*, and *z* bands, respectively. Middle panel: power law + broken power law fits to the <10 days *riz*-band data of AT 2024gsa. The indices for the post-peak decline are steeper after excluding the phase C component, with $\alpha_3 = -2.6 \pm 0.4$, -2.2 ± 0.4, and -2.5 ± 0.1 for *r*, *i*, and *z* bands, respectively. Bottom panel: optical-to-X-ray spectrum of the broadband counterpart of EP 240414a, containing data obtained between 4 and 5 days post-FXT trigger.

We search for other possible frequency-dependent light-curve behavior by fitting the *ri*-band data with a power law to the initial decay phase (i.e., phase A) of the form:

$$F_\nu = At^{\alpha_1}, \tag{1}$$

followed by a broken power law given by:

$$F_\nu = B\left[0.5\left(\frac{t}{t_b}\right)^{s\alpha_2} + 0.5\left(\frac{t}{t_b}\right)^{s\alpha_3}\right]^{1/s}, \tag{2}$$

where F_ν is the flux density, t is the time since FXT, A and B are the amplitudes of the single and broken power-law components, respectively, t_b is the break time of the broken power law, and α_1, α_2, and α_3 are the different temporal power-law exponents. We fit Equation (2) to the *z*-band data, and the resulting fits are shown in Figure 4. The upper panel shows the fits to all the data, while the middle panel shows the fits to all the data obtained <10 days post-FXT (to account for

phase C emission likely being dominated by radiation from the SN).

For all epochs where we have data in at least three bands, we estimate the spectral index, assuming a single-component power law can describe the spectral index. We obtain reasonably good constraints on the spectral index for four epochs between 2 and 15 days post-FXT, ranging between -1.9 and -0.4. At 4 days post-FXT, we have a data point from Swift/XRT in addition to those at optical frequencies, and so we construct a spectral energy distribution (see the bottom panel of Figure 4). The purple shaded region in the bottom panel of Figure 4 denotes the photon index uncertainty on this Swift data point. We fit a single power law to the optical and X-ray data points, and measure a spectral index of -0.76 ± 0.05. When compared to the theoretical spectral index for optically thin synchrotron emission ($\frac{1-p}{2}$), where p typically lies in the range $2 \lesssim p \lesssim 3$, we find that the two are consistent (we measure $p = 2.5 \pm 0.1$).

Given the power-law-like light curves, the nonthermal spectrum of AT 2024gsa, and its high optical luminosity ($M_r \sim -21$), it seems plausible that the optical emission at phases A and B originates from a GRB afterglow. To further explore this possibility, we compare the power-law exponents from the optical light curves to those from analytical models in the literature (e.g., J. Granot & R. Sari 2002; H. Gao et al. 2013).

First, we examine the decay rate measured in the first two days. We find that the initial decay rate is consistent across both bands ($\alpha_1 = -0.31 \pm 0.02$ in r band and $\alpha_1 = -0.33 \pm 0.05$ in i band). We find that this observed decay rate is similar to a forward shock in a fast-cooling, optically thin regime ($\nu_{sa} < \nu_c < \nu_{obs} < \nu_m$), $t^{-0.25}$, and is independent of the circumburst density profile. Here, ν_{sa}, ν_c, ν_{obs}, and ν_m are the self-absorption, cooling, observing, and characteristic electron break frequencies, respectively.

After the peak, we find that the decay rates change significantly depending on whether or not we include the late-time (>10 days post-FXT) data. In the scenario where we include all the data, we find the second decay rate to be steeper: $\alpha_3 = -1.4 \pm 0.4$, -1.04 ± 0.07, and -0.93 ± 0.09 at r, i, and z bands, respectively. When combined with the measured spectral index ($p = 2.5 \pm 0.1$), we find that the optical emission after the light-curve peak is most consistent with a forward shock adiabatically expanding into a homogeneous environment ($\nu_{sa} < \nu_m < \nu_{obs} < \nu_c$; J. Granot & R. Sari 2002).

If we do not include the late-time data points, we find that the post-peak decay rates are even steeper: $\alpha_3 \approx -2.6 \pm 0.4$, -2.2 ± 0.4, and -2.5 ± 0.1 at r, i, and z bands, respectively. These decay rates are consistent with $\alpha_3 = -p$, where p is the same as that derived from the spectral index. In the GRB scenario this is interpreted as an optically thin, post-jet-break decay rate ($\nu_{sa} < \nu_m < \nu_{obs} < \nu_c$; R. Sari et al. 1999). A jet break occurs when the jet has decelerated sufficiently such that the beaming cone encompasses the whole shock front, so the observer sees the intrinsic decay rate of the afterglow. We note that the steeper decay rates are consistent with those found by J. S. Bright et al. (2024b) with ATCA on timescales of tens of days.

From the two decay rates (α_1 and α_3), we can infer that the forward shock transitions from a fast to slow cooling regime (i.e., radiative to adiabatic cooling) between 2 and 3 rest-frame days post-FXT. During the same time period, we observe a rapid rise in the optical light curve. In simple, canonical forward shock models, the steepest possible light-curve rise is $\propto t^{7/4}$ and occurs in the regime $\nu_m < \nu_{obs} < \nu_{sa} < \nu_c$, which does not agree with our findings pre- and post-peak.

Despite the lack of consistency with canonical GRB afterglow models, the observed variability is not uncommon in optical afterglows of GRBs. E.-W. Liang et al. (2013) found a number of GRB afterglows that exhibit optical rebrightening on timescales of $\lesssim$1 day, and a previous Einstein Probe source (EP 240315a) displayed a significant optical and X-ray rebrightening $\approx$3 days post-burst (Y. Liu et al. 2024c). The most likely explanation is that the optical rebrightening is a consequence of refreshed shocks (M. J. Rees & P. Mészáros 1998; R. Sari & P. Mészáros 2000), which result from slower shells ejected from the source after the main burst catching up with and re-energizing the main afterglow shock at late times, as has been suggested for GRB 030329 (J. Granot et al. 2003; M. J. Moss et al. 2023), GRB 160821B (G. P. Lamb et al. 2019), and GRB 170817A (G. P. Lamb et al. 2020). The dynamical timescale in the ejecta is comparable to the time of observation within a decelerating blastwave picture (M. J. Moss et al. 2023). We note that the rebrightening episode during phase B starts at $t \sim 1.5$ rest-frame days with a rise time of $\Delta t \sim 1.5$ rest-frame days, thus satisfying $\Delta t/t \sim 1$. We find that the timescale post-FXT and duration of the flare from AT 2024gsa are very similar to that observed by M. J. Moss et al. (2023). Other plausible mechanisms include external density fluctuations (e.g., Z. G. Dai & T. Lu 2002), although this is difficult to reconcile with such a sharp flux increase (E. Nakar & T. Piran 2003), or possibly magnetar central engine activity (H. Gao et al. 2015). Unfortunately, we do not have comprehensive spectral and temporal coverage to rule out these other scenarios with confidence.

J. S. Bright et al. (2024b) propose that the radio emission detected from EP 240414a is most likely explained by a moderately relativistic outflow that is frequently detected in long GRBs. J. S. Bright et al. (2024b) further note that the only limit on gamma-ray emission at the time of EP 240414a comes from Konus-Wind, and implies $L_{\rm iso} \lesssim 10^{51}\,{\rm erg\,s^{-1}}$ at our measured redshift (A. Tsvetkova et al. 2017). Hence, a low-luminosity GRB may have accompanied EP 240414a, but remained undetected.

5.2. EP 240414a in Context with Other FXTs

EP has released GCNs for 27 FXT events, with 8 optical counterparts discovered, and redshifts measured for just 5 of these.[12] Generally, they appear to be significantly more distant than the redshifts inferred for the XMM-Newton (D. Alp & J. Larsson 2020) and Chandra (J. Quirola-Vásquez et al. 2022, 2023) FXTs. Here, we qualitatively compare the properties of the various samples of FXT objects to explore their similarities and differences. Despite the properties and discovery methods of the Chandra and XMM-Newton FXT samples being distinct from those uncovered by EP, a comparison of their properties can still provide useful insights, as presented below.

Including EP 240414a, there are five FXT events from EP that have known redshifts; these include EP 240315a ($z = 4.859$; J. H. Gillanders et al. 2024; Levan et al. 2024b; Liu et al. 2024c), EP 240414a ($z = 0.4018$; see Section 3),

[12] As of 2024 August 14.

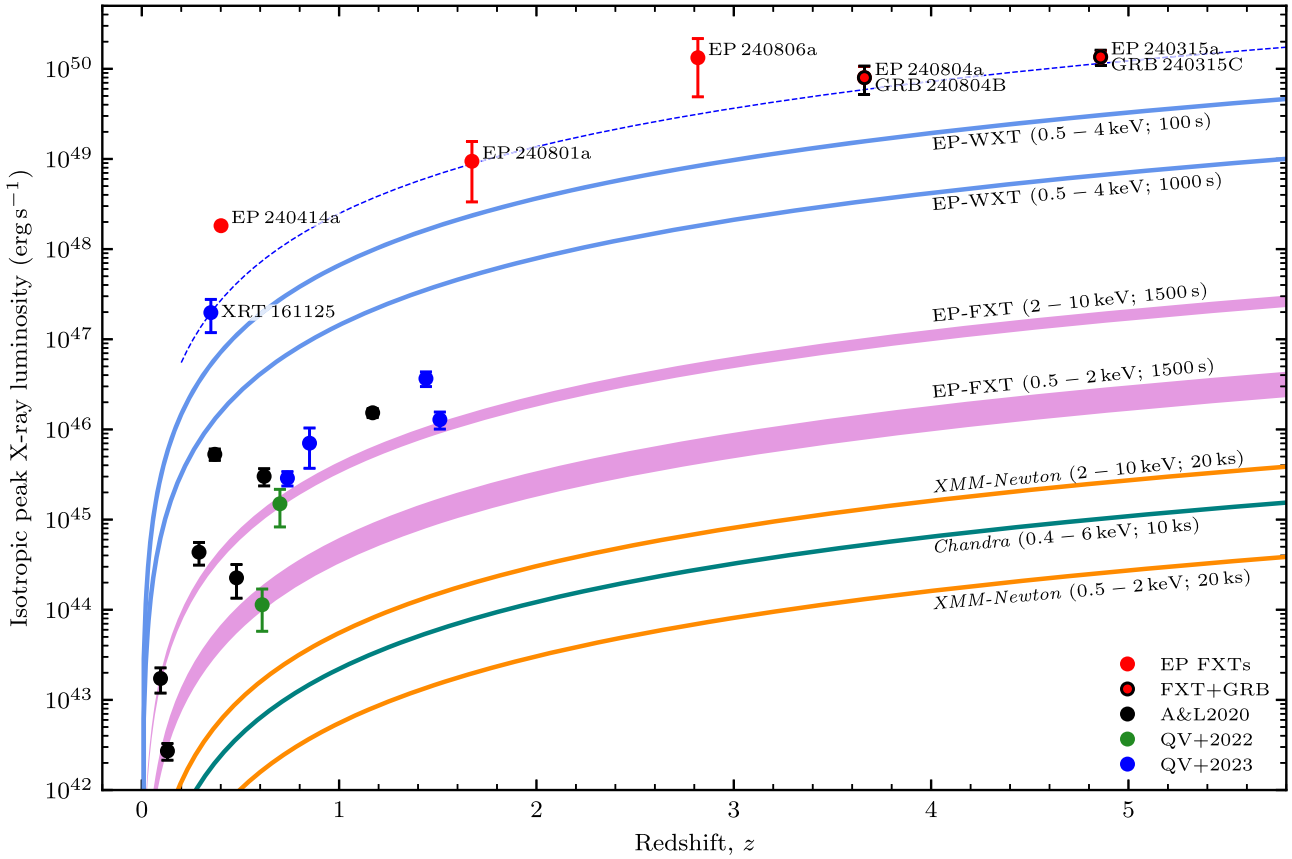

Figure 5. Isotropic peak X-ray luminosities of FXTs as a function of redshift. We compare the sample of EP FXTs with reported redshifts to the A&L2020, QV +2022, and QV+2023 samples (see the main text for details). We highlight the isotropic peak luminosity that XRT 161125 would have, assuming it has a redshift $z \geqslant 0.2$. The simulated sensitivity curves are plotted for EP-WXT and EP-FXT, for the nominal exposure times listed (taken from W. Yuan et al. 2022; J. Zhang et al. 2022). We also plot sensitivity curves for the characteristic detection limits of XMM-Newton and Chandra, taken from M. G. Watson et al. (2001) and the Chandra Observatory guide (https://cxc.harvard.edu/proposer/POG/html/chap6.html).

EP 240801a ($z = 1.673$; J. Quirola-Vásquez et al. 2024a), EP 240804a ($z = 3.662$; A. Bochenek et al. 2024), and EP 240806a ($z = 2.818$; J. Quirola-Vásquez et al. 2024b).

To this set, we add XT 030206, XT 070618, XT 100424, XT 110621, XT 151128, XT 151219, and XT 161028 extracted from the XMM-Newton catalog presented by D. Alp & J. Larsson (2020; hereafter the A&L2020 sample). From archival Chandra observations spanning 2000–2014, we include XRT 041230 and XRT 080819 (J. Quirola-Vásquez et al. 2022; hereafter the QV+2022 sample), and from Chandra observations spanning 2014–2022, we include XRT 150322 (Y. Q. Xue et al. 2019; J. Quirola-Vásquez et al. 2023), XRT 161125 (J. Quirola-Vásquez et al. 2023), XRT 170901 (D. Lin et al. 2019; J. Quirola-Vásquez et al. 2023), XRT 191223 (J. Quirola-Vásquez et al. 2023), and XRT 210423 (D. Lin et al. 2021; J. Quirola-Vásquez et al. 2023), hereafter the QV+2023 sample.

In Figure 5, we compare the EP FXTs to the A&L2020, QV +2022 and QV+2023 samples (D. Alp & J. Larsson 2020; J. Quirola-Vásquez et al. 2022, 2023). For ease of comparison, we convert all recorded peak flux values to isotropic peak luminosity.

From Figure 5 we see that the historical samples of FXTs (i.e., the samples of A&L2020, QV+2022, and QV+2023) all tend to have typical (isotropic-equivalent) luminosities of ∼a few $\times$ 10^{42}–10^{46} erg s^{-1}, and redshifts $z < 1.6$.[13] In comparison, the sample of (known-redshift) EP FXTs are significantly more luminous; they all have $L_{\rm iso} > 10^{48}$ erg s^{-1} and redshifts ranging from $z \approx 0.4$–5. Given that two of these, EP 240315a/GRB 240315C and EP 240804a/GRB 240804B (and 7 of the full sample of 27), are likely the prompt X-ray emission from long GRBs (D. Frederiks et al. 2024; A. J. Levan et al. 2024b; Y. Liu et al. 2024c), this luminosity separation is not unexpected given that we simply compute isotropic luminosity.[14] EP 240414a has a lower luminosity than the high-redshift EP FXTs that are confirmed GRBs, and is at a comparable redshift to the A&L2020, QV+2022, and QV +2023 samples. However, it seems unlikely to be related to the Chandra and XMM-Newton sources as it is more than 2 orders of magnitude more luminous.[15]

Given the EP-WXT observing strategy of $t_{\rm exp} = 900$–1200 s (W. Yuan et al. 2022), a source with $L_{\rm iso} = 10^{45}$ erg s^{-1} would only be detectable at a redshift $z \lesssim 0.1$. Hence, the X-ray luminosity parameter space probed by EP is distinct from that which most previously known FXTs occupy. EP is designed such that it has a higher luminosity threshold than XMM-Newton and Chandra, making it insensitive to the parameter space occupied by the historical FXT samples (see Figure 5 for a visualization of the sensitivity limits of EP, XMM-Newton, and Chandra). Conversely, XMM-Newton and Chandra have not detected FXTs that match those uncovered by EP; this is

[13] The exception to this is XRT 161125, which we discuss later.

[14] Assuming the low-redshift FXT samples are not beamed events.

[15] Aside from XRT 161125.

indicative of EP-detected events being intrinsically (volumetrically) rare events that have been routinely missed by the narrow fields of view of these observatories. However, the large field of view of EP has ensured their detection. Thus, it appears that EP is primarily sensitive to the rare, luminous events that are broadly consistent with cosmological GRB events (out to high z), whereas the deep, narrower-field-of-view observatories are more suited to uncovering intrinsically fainter (but volumetrically more common) FXTs.

The one exception to this broad picture is XRT 161125, which has $L_{\rm iso} = 2 \times 10^{47}\,{\rm erg\,s^{-1}}$ and a redshift $z = 0.35^{+0.05}_{-0.15}$ (J. Quirola-Vásquez et al. 2023). This redshift is based on an unconfirmed association with the marginally resolved $r = 24.2$ mag host galaxy in the DECam Legacy Surveys (A. Dey et al. 2019). Thus, the association is far from secure, and it is plausible that this is merely a chance coincidence (J. Quirola-Vásquez et al. 2023 estimate a chance association probability of <0.095), with XRT 161125 being at a much larger distance, making it similar in physical nature to the high-redshift EP transient sample. In Figure 5, we illustrate where in the luminosity/redshift parameter space XRT 161125 would lie for a range of redshifts ($z \geqslant 0.2$). We find that the isotropic peak luminosity inferred for XRT 161125 closely resembles that of the four EP FXTs at $z \gtrsim 1.5$ (EP 240315a, EP 240801a, EP 240804a, and EP 240806a).

Alternatively, if the host galaxy association for XRT 161125 is correct, then we note that XRT 161125 possesses a (projected) offset of $\approx$13.2 kpc (J. Quirola-Vásquez et al. 2023). This value is approximately half the separation observed here for EP 240414a/AT 2024gsa (27 kpc; see Section 3).

While EP 240414a/AT 2024gsa has a redshift in agreement with the historical sample of FXT events, its relatively high luminosity paired with our light-curve analysis (see Section 4) indicates that this event is consistent with a GRB. In Figure 5, we see that EP 240414a is somewhat fainter than (but close to) the luminosity of the rest of the sample of known-redshift, EP-detected FXT events. We conclude that EP 240414a likely belongs to the same population as these other EP-discovered FXTs, thus making it the most nearby (and intrinsically faintest) FXT event detected by EP linked to a GRB.

6. Summary and Conclusions

This Letter presents the discovery of AT 2024gsa, the optical counterpart to the FXT EP 240414a. The most likely host galaxy is identified as SDSS J124601.99-094309.3, which we show has a redshift $z = 0.4018 \pm 0.0010$, with EP 240414a having a large (projected) radial offset of 27 kpc. We compute the chance coincidence of EP 240414a with SDSS J124601.99 −094309.3 to be $\lesssim$0.01.

Optical photometric follow-up of AT 2024gsa reveals a luminous, multipeaked light curve. Three distinct phases are identified: $\lesssim$2, 2–10, and $\gtrsim$10 rest-frame days post-FXT (phases A, B, and C, respectively).

Phase A rapidly fades from an initial discovery AB magnitude $M_i \approx -20.4$ to $M_i \approx -19.5$ within 1.5 (rest-frame) days, before rebrightening on a $\sim$0.5 day timescale to $M_i \sim -21$. This second phase (B) then declines over a $\sim$ 10 day period, before transitioning into the slowly evolving phase C. We find that phases A and B can be readily explained with a combination of simple power-law fits, indicating the plausibility of the early light curve being powered by GRB afterglow radiation (with some rebrightening effects).

Although the rapid timescale and high luminosity ($M_r \sim -21$) of phase B is reminiscent of LFBOTs, we do not favor this scenario of thermal emission based on detailed analysis with MOSFiT that yields inferred ejecta velocities of $0.8 \lesssim v_{\rm ej}/c \lesssim 0.9$. The high X-ray luminosity, together with the red optical colors and achromatic evolution, support a nonthermal powering mechanism. A spectral energy distribution fit to the composite optical and Swift/XRT data during phase B yields a spectral index of 0.76 ± 0.05, consistent with optically thin synchrotron emission.

The third phase (C), starting $\sim$10 rest-frame days post-FXT, shows evidence of an emerging SN component, the timescale and luminosity of which is consistent with broad-line SNe Ic, lending further support to a long GRB interpretation.

By comparing the full sample of known-redshift EP-discovered FXTs with the historical XMM-Newton and Chandra samples of FXTs, we find that EP-FXT events are consistently and systematically more luminous than all previously discovered FXTs. EP 240414a is the most nearby of the EP-discovered FXT sample to date by a considerable margin, and, although its redshift closely resembles the XMM-Newton and Chandra samples, it is significantly more luminous. EP is optimized for uncovering volumetrically rare, high-redshift, X-ray-luminous events, many of which appear to be linked to gamma-ray bursts.

EP 240414a is likely X-ray emission from a low-luminosity GRB, with the early optical observations dominated by afterglow, followed by thermal emission from a GRB-SN. EP 240414a is thus the lowest luminosity, and most nearby, EP-discovered FXT+GRB event uncovered to date.

Acknowledgments

The authors thank the anonymous reviewer for detailed comments that improved the quality of the manuscript.

S.J.S., S.S., K.W.S., and D.R.Y. acknowledge funding from STFC grants ST/Y001605/1, ST/X001253/1, ST/X006506/1, and ST/T000198/1. S.J.S. acknowledges a Royal Society Research Professorship and the Hintze Charitable Foundation. H.F.S. is supported by Schmidt Sciences, LLC. L.R. acknowledges support from the Canada Excellence Research Chair in Transient Astrophysics (CERC-2022-00009). M.N. is supported by the European Research Council (ERC) under the European Union's Horizon 2020 research and innovation program (grant agreement No. 948381) and by UK Space Agency grant No. ST/Y000692/1. F.C. acknowledges support from the Royal Society through the Newton International Fellowship program (NIF/R1/211296). A.J.C. acknowledges support from the Hintze Family Charitable Foundation. T.W.C. and A.A. acknowledge the Yushan Fellow Program by the Ministry of Education, Taiwan, for financial support (MOE-111-YSFMS-0008-001-P1). S.Y. acknowledges the funding from the National Natural Science Foundation of China under grant No. 12303046 and the Henan Province High-Level Talent International Training Program. A.B. is grateful to the Royal Society, United Kingdom, and also acknowledges SERB (SB/SRS/2022-23/124/PS) for financial support.

Pan-STARRS is primarily funded to search for near-Earth asteroids through NASA grants NNX08AR22G and NNX14AM74G. The Pan-STARRS science products for transient follow-up are made possible through the contributions of the University of Hawaii Institute for Astronomy and Queen's University Belfast.

This publication has made use of data collected at Lulin Observatory, partly supported by MoST grant 108-2112-M-008-001. We thank Lulin staff and NCU-GREAT team members for observations.

The Liverpool Telescope is operated on the island of La Palma by Liverpool John Moores University in the Spanish Observatorio del Roque de los Muchachos of the Instituto de Astrofisica de Canarias with financial support from the UK Science and Technology Facilities Council.

Based on observations obtained at the international Gemini Observatory (under program IDs GN-2024A-Q-128 and GS-2024A-DD-201), a program of NSF NOIRLab, which is managed by the Association of Universities for Research in Astronomy (AURA) under a cooperative agreement with the U.S. National Science Foundation on behalf of the Gemini Observatory partnership: the U.S. National Science Foundation (United States), National Research Council (Canada), Agencia Nacional de Investigación y Desarrollo (Chile), Ministerio de Ciencia, Tecnologìa e Innovación (Argentina), Ministério da Ciência, Tecnologia, Inovações e Comunicações (Brazil), and Korea Astronomy and Space Science Institute (Republic of Korea). This work was enabled by observations made from the Gemini-North telescope, located within the Maunakea Science Reserve and adjacent to the summit of Maunakea. We are grateful for the privilege of observing the Universe from a place that is unique in both its astronomical quality and its cultural significance.

Facilities: LO:1m, PS1, Gemini:Gillett, Gemini:South.

Software: `Astropy` (Astropy Collaboration et al. 2013, 2018, 2022), `Matplotlib` (J. D. Hunter 2007), `NumPy` (C. R. Harris et al. 2020), `pandas` (W. McKinney 2010; pandas development team 2020), `DRAGONS` (K. Labrie et al. 2023a, 2023b).

Appendix A
Optical Counterpart Follow-up

A.1. Historical Nondetections of an Optical Excess in ATLAS and Pan-STARRS

We checked the survey history of the Asteroid Terrestrial-impact Last Alert System (ATLAS; J. L. Tonry et al. 2018) at this sky position for any excess flux before the EP X-ray discovery, or for outbursts from the source that may suggest a Galactic flaring star in chance coincidence with the putative host galaxy. The ATLAS system is composed of four 0.5 m telescopes that provide continuous sky coverage. ATLAS typically images the visible sky four times in 24 hr when all four units are operating, and all data are processed rapidly to search for extragalactic transients (K. W. Smith et al. 2020). The last observations of this position with ATLAS were 5×30 s exposures obtained between MJDs 60402 and 60404 with the Sutherland unit in South Africa, with a stacked 3σ forced upper limit of $o > 21.6$ measured from the difference images. There is no indication of any activity in the survey history of ATLAS. There is also no indication of a flux excess in forced photometry at this position in the history of Pan-STARRS survey data in 194 separate images between 2017 March 17 and 2024 March 19, to typical AB magnitudes of $w_{\rm PS} \gtrsim 22$.

A.2. Optical Photometric Follow-up

After the initial discovery, we continued to obtain follow-up photometry of AT 2024gsa with the LOT in *gri* bands. We employed the Kinder pipeline (S. Yang et al. 2021) to conduct point-spread function (PSF) photometry for AT 2024gsa with template subtraction. The derived magnitudes and upper limits were determined by calibrating against SDSS field stars in the AB system.

Additionally, follow-up photometric observations with Pan-STARRS commenced on MJD 60416.41, 2.0 days after the discovery of EP 240414a. Pan-STARRS (PS) comprises a twin 1.8 m telescope system (Pan-STARRS1 and Pan-STARRS2), both situated atop Haleakala mountain on the Hawaiian island of Maui (K. C. Chambers et al. 2016). Images of AT 2024gsa were obtained with Pan-STARRS1 (PS1), equipped with a 1.4 gigapixel camera and a $0\farcs26$ pixel scale, providing a ~ 7 deg^2 field of view. The images were obtained in the *grizy* filters (J. L. Tonry et al. 2012). Images were processed with the Image Processing Pipeline (E. A. Magnier et al. 2020a; C. Z. Waters et al. 2020). The images were astrometrically and photometrically calibrated (E. A. Magnier et al. 2020b) and individual frames were coadded with median clipping to produce stacks, on which PSF photometry was performed (E. A. Magnier et al. 2020c).

Finally, we obtained *riz*-band images with the Gemini-North/GMOS-N instrument commencing on MJD 60489.28 ($\sim$75 days after the FXT trigger), under the program ID GN-2024A-Q-128 (PI: M. Huber). We also obtained images of the field in *i* band with Gemini-South/GMOS-S starting MJD 60507.98 ($\sim$94 days post-FXT) under a Director's Discretionary Time proposal (PI: S. J. Smartt). These images were reduced using the `DRAGONS` pipeline (K. Labrie et al. 2023a, 2023b) and following standard recipes. The GMOS images are considerably deeper than reference images of the field from PS1, and image subtraction was therefore not possible. Although AT 2024gsa is detected in the first set of GMOS images on MJD 60489 (see Figure 1, lower-left panel), the transient is faint and host contamination is quite significant at the location. We used the `PSF` code (M. Nicholl et al. 2023) to perform photometry on the GMOS images without subtraction, and the estimated magnitudes are likely overestimated due to host galaxy contamination, particularly in the *z* band.

The optical light curve is shown in Figure 3 and the summary of photometric observations is provided in Table 1.

A.3. Swift X-Ray Analysis

The EP-WXT detection was reported by T. Y. Lian et al. (2024) as a trigger starting 2024 April 14 at 09:50:12 UTC (MJD 60414.40986), with a peak flux of $\sim 3 \times 10^{-9}$ erg s^{-1} cm^{-2} in the 0.5–4 keV band. This was followed up with the EP-FXT observation starting on 2024 April 14 at 11:50:01 UTC, approximately 2 hr after the EP-WXT detection (J. Guan et al. 2024). The derived unabsorbed flux was reported by J. Guan et al. (2024) to be $3.5 \pm 0.8 \times 10^{-13}$ erg s^{-1} cm^{-2} in the 0.5–10 keV band; the source was seen to have rapidly faded.[16]

After the initial detection of EP 240414a, three Swift/XRT observations were performed in photon counting mode. The

[16] J. Guan et al. (2024) obtained this value by fitting the X-ray EP-FXT spectrum with an absorbed power-law model, invoking $N_{\rm H} = 3.35 \times 10^{20}$ cm^{-2} and a photon index of 1.7 ± 0.3.

first observation made on 2024 April 18 detected a low number of photons, and, therefore, did not allow us to invoke χ^2 statistics. We grouped the spectra using the ftools task `grppha` (*HEASoft* v6.33.2) to have at least 1 count per bin. Spectra were fitted using XSPEC 12.14.0H (K. A. Arnaud 1996). Using W-statistics and background-subtracted Cash statistics (K. Wachter et al. 1979), we fit the spectra using an absorbed power-law model. Owing to limited statistics, it was difficult to constrain $N_{\rm H}$ and the photon index. Therefore, we fixed these values to that reported by J. Guan et al. (2024). The obtained X-ray flux ($5 \pm 2 \times 10^{-13}$ erg s^{-1} cm^{-2}; 0.3 − 10 keV) was found to be consistent with that reported by the EP team. Due to the rapid decay of the source in X-rays, it was not possible to fit the spectra of the other two observations made on 2024 April 24 and 27. Therefore, we combined data of these two observations and computed a 95% confidence level upper limit count rate using the prescription given by N. Gehrels (1986); the corresponding flux value was found to be 2.25×10^{-13} erg s^{-1} cm^{-2} using the WEBPIMMS HEASARC tool, assuming a photon index of 2.

Appendix B
Color Evolution of AT 2024gsa

Here, we include a visual demonstration of the intrinsically red color of AT 2024gsa, compared with AT 2018cow (S. J. Prentice et al. 2018), GRB 071010A (S. Covino et al. 2008), and SN 1998bw (A. Clocchiatti et al. 2011; Figure 6). It is apparent that AT 2024gsa is significantly redder than the LFBOT AT 2018cow and also SN 1998bw at later times. The early color evolution of AT 2024gsa is somewhat similar to SN 1998bw; however, the luminosity is much higher relative to SN 1998bw at a similar epoch (see Section 4 for more details).

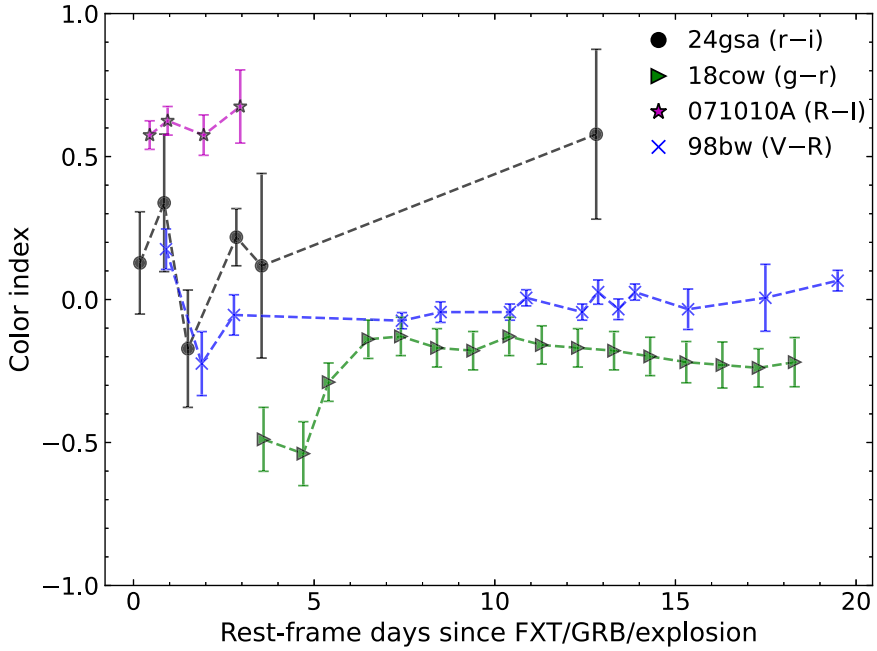

Figure 6. The ($r - i$) color evolution of AT 2024gsa at early times (phases A and B), compared to the ($g - r$) color evolution of AT 2018cow (S. J. Prentice et al. 2018), ($R - I$) color evolution of GRB 071010A (S. Covino et al. 2008), and ($V - R$) color evolution of SN 1998bw (A. Clocchiatti et al. 2011).

ORCID iDs

S. Srivastav https://orcid.org/0000-0003-4524-6883
T.-W. Chen https://orcid.org/0000-0002-1066-6098
J. H. Gillanders https://orcid.org/0000-0002-8094-6108
L. Rhodes https://orcid.org/0000-0003-2705-4941
S. J. Smartt https://orcid.org/0000-0002-8229-1731
M. E. Huber https://orcid.org/0000-0003-1059-9603
A. Aryan https://orcid.org/0000-0002-9928-0369
S. Yang https://orcid.org/0000-0002-2898-6532
A. Beri https://orcid.org/0000-0003-3753-3102
A. J. Cooper https://orcid.org/0000-0002-4033-3139
M. Nicholl https://orcid.org/0000-0002-2555-3192
K. W. Smith https://orcid.org/0000-0001-9535-3199
H. F. Stevance https://orcid.org/0000-0002-0504-4323
F. Carotenuto https://orcid.org/0000-0002-0426-3276
K. C. Chambers https://orcid.org/0000-0001-6965-7789
A. Aamer https://orcid.org/0000-0002-9085-8187
C.R. Angus https://orcid.org/0000-0002-4269-7999
M. D. Fulton https://orcid.org/0000-0003-1916-0664
T. Moore https://orcid.org/0000-0001-8385-3727
I. A. Smith https://orcid.org/0000-0001-8605-5608
D. R. Young https://orcid.org/0000-0002-1229-2499
T. de Boer https://orcid.org/0000-0001-5486-2747
H. Gao https://orcid.org/0000-0003-1015-5367
C.-C. Lin https://orcid.org/0000-0002-7272-5129
T. Lowe https://orcid.org/0000-0002-9438-3617
E. A. Magnier https://orcid.org/0000-0002-7965-2815
Y.-C. Pan https://orcid.org/0000-0001-8415-6720
R. J. Wainscoat https://orcid.org/0000-0002-1341-0952

References

Aguado, D. S., Ahumada, R., Almeida, A., et al. 2019, ApJS, 240, 23
Ai, S., & Zhang, B. 2021, ApJL, 915, L11
Alp, D., & Larsson, J. 2020, ApJ, 896, 39
Arnaud, K. A. 1996, ASP Conf. Ser. 101, Astronomical Data Analysis Software and Systems V, ed. G. H. Jacoby & J. Barnes, (San Francisco, CA: ASP), 17
Aryan, A., Yang, S., Chen, T. W., et al. 2024a, GCN, 36094, 1
Aryan, A., Yang, S., Chen, T. W., et al. 2024b, TNSTR, 2024, 1
Astropy Collaboration, Robitaille, T. P., Tollerud, E. J., et al. 2013, A&A, 558, A33
Astropy Collaboration, Price-Whelan, A. M., Sipocz, B. M., et al. 2018, AJ, 156, 123
Astropy Collaboration, Price-Whelan, A. M., Lim, P. L., et al. 2022, ApJ, 935, 167
Bauer, F. E., Treister, E., Schawinski, K., et al. 2017, MNRAS, 467, 4841
Bloom, J. S., Kulkarni, S. R., & Djorgovski, S. G. 2002, AJ, 123, 1111
Bochenek, A., Xu, D., Zhu, Z., et al. 2024, GCN, 37039, 1
Bright, J., Carotenuto, F., Jonker, P. G., Fender, R., & Smartt, S. 2024a, GCN, 36362, 1
Bright, J. S., Carotenuto, F., Fender, R., et al. 2024b, arXiv:2409.19055
Chambers, K. C., Magnier, E. A., Metcalfe, N., et al. 2016, arXiv:1612.05560
Chen, T. W., Yang, S., Pan, Y. C., et al. 2021, TNSAN, 92, 1
Chen, T.-W., Yang, S., Srivastav, S., et al. 2024, arXiv:2406.09270
Clocchiatti, A., Suntzeff, N. B., Covarrubias, R., & Candia, P. 2011, AJ, 141, 163
Covino, S., D'Avanzo, P., Klotz, A., et al. 2008, MNRAS, 388, 347
Dai, Z. G., & Lu, T. 2002, ApJL, 565, L87
DeLaunay, J., Tohuvavohu, A., Svinkin, D., et al. 2024, GCN, 35971, 1
Dey, A., Schlegel, D. J., Lang, D., et al. 2019, AJ, 157, 168
Eappachen, D., Jonker, P. G., Levan, A. J., et al. 2023, ApJ, 948, 91
Eappachen, D., Jonker, P. G., Quirola-Vásquez, J., et al. 2024, MNRAS, 527, 11823
Flewelling, H. A., Magnier, E. A., Chambers, K. C., et al. 2020, ApJS, 251, 7
Frederiks, D., Lysenko, A., Ridnaia, A., et al. 2024, GCN, 37071, 1
Gao, H., Ding, X., Wu, X.-F., Dai, Z.-G., & Zhang, B. 2015, ApJ, 807, 163
Gao, H., Lei, W.-H., Zou, Y.-C., Wu, X.-F., & Zhang, B. 2013, NewAR, 57, 141
Gehrels, N. 1986, ApJ, 303, 336
Gillanders, J. H., Rhodes, L., Srivastav, S., et al. 2024, ApJL, 969, L14
Glennie, A., Jonker, P. G., Fender, R. P., Nagayama, T., & Pretorius, M. L. 2015, MNRAS, 450, 3765
Granot, J., Nakar, E., & Piran, T. 2003, Natur, 426, 138
Granot, J., & Sari, R. 2002, ApJ, 568, 820
Guan, J., Li, C. K., Chen, Y., et al. 2024, GCN, 36129, 1
Guillochon, J., Nicholl, M., Villar, V. A., et al. 2018, ApJS, 236, 6
Hanuschik, R. W. 2003, A&A, 407, 1157
Harris, C. R., Millman, K. J., van der Walt, S. J., et al. 2020, Natur, 585, 357
Hunter, J. D. 2007, CSE, 9, 90
Jonker, P. G., Levan, A. J., Malesani, D. B., et al. 2024, GCN, 36110, 1
Jonker, P. G., Glennie, A., Heida, M., et al. 2013, ApJ, 779, 14
Kasen, D., & Bildsten, L. 2010, ApJ, 717, 245
Labrie, K., Simpson, C., Cardenes, R., et al. 2023a, RNAAS, 7, 214
Labrie, K., Simpson, C., Turner, J., et al. 2023b, DRAGONS, v3.1.0, Zenodo, doi: 10.5281/zenodo.7776065
Lamb, G. P., Levan, A. J., & Tanvir, N. R. 2020, ApJ, 899, 105
Lamb, G. P., Tanvir, N. R., Levan, A. J., et al. 2019, ApJ, 883, 48
Levan, A. J., van Dalen, J., Jonker, P., et al. 2024a, GCN, 36355, 1
Levan, A. J., Jonker, P. G., Saccardi, A., et al. 2024b, arXiv:2404.16350
Lian, T. Y., Pan, X., Ling, Z. X., et al. 2024, GCN, 36091, 1
Liang, E.-W., Li, L., Gao, H., et al. 2013, ApJ, 774, 13
Lin, D., Irwin, J., & Berger, E. 2019, ATel, 13171, 1
Lin, D., Irwin, J. A., & Berger, E. 2021, ATel, 14599, 1
Ling, Z. X., Liu, M. J., Liu, Y., et al. 2024, ATel, 16546, 1
Liu, M. J., Li, D. Y., Liu, Y., et al. 2024a, ATel, 16514, 1
Liu, Y., Liu, M. J., Cheng, H. Q., et al. 2024b, ATel, 16509, 1
Liu, Y., Sun, H., Xu, D., et al. 2024c, arXiv:2404.16425
MacLeod, M., Trenti, M., & Ramirez-Ruiz, E. 2016, ApJ, 819, 70
Magnier, E. A., Chambers, K. C., Flewelling, H. A., et al. 2020a, ApJS, 251, 3
Magnier, E. A., Schlafly, E. F., Finkbeiner, D. P., et al. 2020b, ApJS, 251, 6
Magnier, E. A., Sweeney, W. E., Chambers, K. C., et al. 2020c, ApJS, 251, 5
McKinney, W. 2010, Proc. 9th Python in Science Conf., ed. S. van der Walt & J. Millman, 56
Monageng, I. M., Charles, P. A., Buckley, D. A. H., et al. 2024, ATel, 16529, 1
Moss, M. J., Mochkovitch, R., Daigne, F., Beniamini, P., & Guiriec, S. 2023, MNRAS, 525, 5224
Nadyozhin, D. K. 1994, ApJS, 92, 527
Nakar, E., & Piran, T. 2003, ApJ, 598, 400
Nicholl, M. 2018, RNAAS, 2, 230
Nicholl, M., Guillochon, J., & Berger, E. 2017, ApJ, 850, 55
Nicholl, M., Srivastav, S., Fulton, M. D., et al. 2023, ApJL, 954, L28
pandas development team 2020, pandas-dev/pandas: Pandas, latest, Zenodo, doi: 10.5281/zenodo.3509134
Perley, D. A., Mazzali, P. A., Yan, L., et al. 2019, MNRAS, 484, 1031
Planck Collaboration, Ade, P. A. R., Aghanim, N., et al. 2016, A&A, 594, A13
Prentice, S. J., Maguire, K., Smartt, S. J., et al. 2018, ApJL, 865, L3
Quirola-Vásquez, J., Bauer, F. E., Jonker, P. G., et al. 2022, A&A, 663, A168
Quirola-Vásquez, J., Bauer, F. E., Jonker, P. G., et al. 2023, A&A, 675, A44
Quirola-Vásquez, J., van Dalen, J., Malesani, D. B., et al. 2024a, GCN, 37013, 1
Quirola-Vásquez, J., Jonker, P. G., Levan, A. J. ., et al. 2024b, GCN, 37087, 1
Quirola-Vásquez, J., Bauer, F. E., Jonker, P. G., et al. 2024c, A&A, 683, A243
Rees, M. J., & Mészáros, P. 1998, ApJL, 496, L1
Sari, R., & Mészáros, P. 2000, ApJL, 535, L33
Sari, R., Piran, T., & Halpern, J. P. 1999, ApJL, 519, L17
Sarin, N., Ashton, G., Lasky, P. D., et al. 2021, arXiv:2105.10108
Schlafly, E. F., & Finkbeiner, D. P. 2011, ApJ, 737, 103
Smith, K. W., Smartt, S. J., Young, D. R., et al. 2020, PASP, 132, 085002
Srivastav, S., Gillanders, J. H., Rhodes, L., et al. 2024, GCN, 36150, 1
Svinkin, D., Frederiks, D., Lysenko, A., et al. 2024, GCN, 35972, 1
Tonry, J. L., Stubbs, C. W., Kilic, M., et al. 2012, ApJ, 745, 42
Tonry, J. L., Denneau, L., Heinze, A. N., et al. 2018, PASP, 130, 064505
Tsvetkova, A., Frederiks, D., Golenetskii, S., et al. 2017, ApJ, 850, 161
van Dalen, J. N. D., Levan, A. J., Jonker, P. G., et al. 2024, arXiv:2409.19056
Wachter, K., Leach, R., & Kellogg, E. 1979, ApJ, 230, 274
Waters, C. Z., Magnier, E. A., Price, P. A., et al. 2020, ApJS, 251, 4
Watson, M. G., Auguères, J. L., Ballet, J., et al. 2001, A&A, 365, L51
Waxman, E., & Katz, B. 2017, in Handbook of Supernovae, ed. A. W. Alsabti & P. Murdin (Berlin: Springer), 967
Woosley, S. E., Eastman, R. G., & Schmidt, B. P. 1999, ApJ, 516, 788
Xu, D., Malesani, D. B., Jonker, P., et al. 2024, GCN, 36105, 1
Xue, Y. Q., Zheng, X. C., Li, Y., et al. 2019, Natur, 568, 198
Yang, S., Sollerman, J., Chen, T. W., et al. 2021, A&A, 646, A22
Yuan, W., Zhang, C., Chen, Y., & Ling, Z. 2022, The Einstein Probe Mission (Singapore: Springer), 1
Zhang, C., Ling, Z. X., Liu, Y., et al. 2024, ATel, 16463, 1
Zhang, J., Qi, L., Yang, Y., et al. 2022, APh, 137, 102668
Zhang, W. J., Mao, X., Zhang, W. D., et al. 2024, GCN, 35931, 1